

# One-pass Multi-task Networks with Cross-task Guided Attention for Brain Tumor Segmentation

Chenhong Zhou, Changxing Ding, Xinchao Wang, Zhentai Lu, Dacheng Tao

**Abstract**—Class imbalance has been one of the major challenges for medical image segmentation. The model cascade (MC) strategy, as a popular scheme, significantly alleviates class imbalance issue via running a set of individual deep models for coarse-to-fine segmentation. In spite of its outstanding performance, this method leads to an undesired system complexity and meanwhile ignores the relevance among the models. To handle these flaws of MC, we propose in this paper a light-weight deep model, i.e., the One-pass Multi-task Network (OM-Net) to solve class imbalance better than MC and require only one-pass computation for brain tumor segmentation. First, OM-Net integrates the separate segmentation tasks into one deep model, which consists of shared parameters to learn joint features and task-specific parameters to learn discriminative features. Second, to optimize OM-Net more effectively, we take advantage of the correlation among tasks to design an online training data transfer strategy and a curriculum learning-based training strategy. Third, we further propose to share prediction results between tasks, which enables us to design a cross-task guided attention (CGA) module. With the guidance of prediction results provided by the previous task, CGA can adaptively recalibrate channel-wise feature responses based on the category-specific statistics. Finally, a simple yet effective post-processing method is introduced to refine the segmentation results of the proposed attention network. Extensive experiments are performed to justify the effectiveness of the proposed techniques. Most impressively, we achieve state-of-the-art performance on the BraTS 2015 testing set and BraTS 2017 online validation set. With the proposed approaches, we also won the joint third place in the BraTS 2018 challenge among 64 participating teams. We will make the code publicly available at <https://github.com/chenhong-zhou/OM-Net>.

**Index Terms**—Brain tumor segmentation, magnetic resonance imaging, class imbalance, convolutional neural networks, multi-task learning, channel attention.

## I. INTRODUCTION

**B**RAIN tumors are one of the most deadly cancers worldwide, among which glioma is the most common type [1]. The average survival time for glioblastoma patients is less than 14 months [2]. Timely diagnosis of brain tumors is thus vital for treatment planning, surgery, and follow-up visits [3]. As a popular non-invasive technique, Magnetic Resonance

Imaging (MRI) produces markedly different types of tissue contrast, and has been widely used by radiologists to diagnose brain tumors [4]. The manual segmentation of brain tumors from MRI images is, however, subjective and meanwhile time-consuming [5]. Therefore, it is highly desirable to design automatic and robust brain tumor segmentation tools.

Recently, deep learning-based methods, e.g., convolutional neural networks (CNNs) [5]–[17], have been increasingly popular and achieved great progress in brain tumor segmentation. Unfortunately, there is usually a severe class imbalance problem between healthy tissue and tumor tissue as well as intra-tumoral classes. This problem causes the healthy tissue being dominant during the training phase and degrades the optimization quality of the model. To handle the class imbalance problem, many recent studies employ the Model Cascade (MC) strategy [18]–[26], which effectively alleviates class imbalance via coarse-to-fine segmentation. In spite of its effectiveness, MC has the following disadvantages. First, it usually requires training multiple deep models, which largely increases the system complexity and the storage space consumption. Second, each model is trained separately using its own training data, which ignores the correlation between the deep models. Third, MC runs the deep models one-by-one, which leads to alternate GPU-CPU computations and lacks online interactions between tasks.

Here we propose to adopt multi-task learning to overcome the shortcomings of MC. Specifically, we decompose the multi-class brain tumor segmentation into three individual yet relevant tasks. Unlike training one individual network for each task in MC, we incorporate the three tasks into a single model and propose a One-pass Multi-task Network (OM-Net). This strategy not only makes use of their relevance during the training stage but also simplifies the prediction stage by one-pass computation. Furthermore, an effective training scheme inspired by curriculum learning is designed: instead of training the three tasks together all the time, we gradually add the tasks in an increasing order of difficulty to OM-Net, which is beneficial to improving the convergence quality of the model.

OM-Net integrating three tasks provides the possibility of online interaction between tasks, which produces more benefits. First, the online training data transfer strategy we proposed here, enables the three tasks in OM-Net to share training data. Therefore, certain tasks obtain more training data and the optimization quality can be improved. Second, we construct a novel channel attention module named Cross-task Guided Attention (CGA), via sharing prediction results between tasks. In the CGA, prediction results of one preceding task can guide its following task to obtain category-specific statistics for

C. Zhou and C. Ding are with the School of Electronic and Information Engineering, South China University of Technology, Guangzhou, China. E-mail: eezhouch@mail.scut.edu.cn, chxding@scut.edu.cn.

X. Wang is with Department of Computer Science, Stevens Institute of Technology, Hoboken, USA.

Z. Lu is with Guangdong Provincial Key Laboratory of Medical Image Processing, School of Biomedical Engineering, Southern Medical University, Guangzhou, China.

D. Tao is with the UBTech Sydney Artificial Intelligence Centre and the School of Information Technologies, Faculty of Engineering and Information Technologies, The University of Sydney, Sydney, Australia. E-mail: dacheng.tao@sydney.edu.au.

each channel beforehand. The category-specific information further enables CGA to predict channel-wise dependencies with regard to one specific category of voxels, respectively. In contrast, existing self-attention models, e.g., the popular ‘squeeze & excitation’ (SE) block [27], do not make use of such external guidance. Without external guidance, SE blocks only predict one single weight for each channel. However, there are usually multiple categories in a patch and the importance of each channel for different categories varies. The proposed CGA module handles this problem by predicting the category-specific channel attention.

To further refine the segmentation results of OM-Net, we also propose a new post-processing scheme. Efficacy of the proposed methods is systematically evaluated on three popular datasets for brain tumor segmentation, i.e., BraTS 2015, 2017, and 2018. Experimental results indicate that OM-Net outperforms MC, yet with only one-third of the model parameters of MC. The CGA module further promotes the performance of OM-Net with a significant margin.

A preliminary version of this paper has been published in [28]. Compared with the conference version, this version proposes the novel CGA module, improves the post-processing method, and includes more experimental investigation. The remainder of the paper is organized as follows. We briefly review the related works for brain tumor segmentation in Section II, and provide the details of OM-Net model in Section III. Experimental settings and datasets are detailed in Section IV, with experimental results and analysis presented in Section V. We conclude the paper in Section VI.

## II. RELATED WORKS

Here we briefly review approaches in two domains that are related to ours: the ones in brain tumor segmentation, and those in attention mechanism.

### A. Brain Tumor Segmentation

In recent years, deep learning-based methods, such as CNNs, have dominated the field of automatic brain tumor segmentation. Architectures for deep models [5]–[17] have rapidly developed from single-label prediction (classifying the central voxel of the input patch only) to dense-prediction (making predictions for all voxels simultaneously in the input patch). For instance, Pereira *et al.* [5] designed a deep model equipped with small convolutional kernels to classify the central voxel of the input 2D patch. Havaei *et al.* [6] introduced a novel 2D two-pathway deep model to explore more contextual information. The above methods make predictions based on 2D patches, ignoring the 3D contextual information. To handle this problem, Kamnitsas *et al.* [7] introduced the DeepMedic model that extracts information from 3D patches using 3D convolutional kernels. The above methods make predictions for a single or a set of central voxels only within the input patch; therefore, they are slow in the inference stage. To promote efficiency, encoder-decoder architectures, e.g., fully convolutional networks (FCNs) [8] and U-Net [9], have been widely adopted to realize dense prediction. For instance, Chen *et al.* [10] designed a voxelwise residual network (VoxResNet)

to make predictions for all voxels within the input 3D patch. Zhao *et al.* [11] introduced a unified framework integrating FCNs and conditional random fields (CRFs) [29]. This framework realizes end-to-end dense prediction with appearance and spatial consistency.

Class imbalance is a commonly encountered issue in medical image segmentation, especially for brain tumor segmentation. To address this problem, many recent studies adopt the MC strategy [18]–[26] to perform coarse-to-fine segmentation. MC decomposes medical image segmentation into two or more tasks, in which each task is achieved by an individual model. The most common MC framework incorporates two models, where the first one detects regions of interest (ROIs) as coarse segmentation, and the second one conducts fine segmentation within the ROIs. This framework has been widely adopted in many applications, e.g., renal segmentation in dynamic contrast-enhanced MRI (DCE-MRI) images [18], cancer cell detection in phase contrast microscopy images [19], liver and lesion segmentation [20], volumetric pancreas segmentation in CT images [21], and calcium scoring in low-dose chest CT images [22], etc. MC can incorporate more stages to achieve better segmentation performance. For instance, Wang *et al.* [23] divided the brain tumor segmentation into three successive binary segmentation problems, i.e., the segmentation of the complete tumor, tumor core, and enhancing tumor areas in MRI, respectively. Since MC effectively alleviates class imbalance, its results are very encouraging.

Despite its effectiveness, MC is cumbersome in terms of system complexity. Moreover, it ignores the correlation among tasks. In this paper, we adopt multi-task learning to overcome the disadvantages of MC. By sharing model parameters and training data, OM-Net outperforms MC, with only one-third model parameters of MC.

### B. Attention Mechanism

Attention is a popular tool in deep learning that highlights useful information in feature maps while suppressing irrelevant counterparts. The majority of existing studies [27], [30]–[37] belong to self-attention models, meaning that they infer attentions based on feature maps only. They can be roughly categorized into three types, i.e., hard regional attention, soft spatial attention, and channel attention. There are also studies that combine two or more types of attention in one unified model [31]–[34]. Spatial transformer network (STN) [30] is, for example, a representative hard attention model. STN selects and reshapes important regions in feature maps to a canonical pose to simplify inference. STN performs at the coarse region-level while neglecting the fine pixel-level saliency [31]. In comparison, soft spatial attention models aim to evaluate pixel-wise importance in the spatial dimension. For instance, Wang *et al.* [32] introduced the residual attention learning method that adds soft weights on feature maps by a residual unit, so as to refine the feature maps.

Complementary to spatial attention, channel attention aims to recalibrate channel-wise feature responses. The ‘squeeze & excitation’ (SE) block [27] is one of the most popular channel attention models due to its simplicity and efficiency. However,

it was originally proposed for image classification and object detection tasks, but may not be optimal for image segmentation task. This is because SE blocks are based on the average response of all voxels in each channel and then recalibrate each channel with a single weight, regardless of the category of voxels. However, there are usually multiple categories of voxels in one patch, and the importance of each channel varies for different categories. There are already studies that have tried to alleviate the above problems of SE blocks for the segmentation task. For example, Pereira *et al.* [35] designed a segmentation SE (SegSE) block which predicts one separate channel attention for each voxel in feature maps; therefore, the obtained channel attention map is of the same size as the feature maps. Voxel-wise multiplication between the feature maps and the attention map produces the re-weighted features.

The proposed CGA module also aims to solve the problems of SE blocks for segmentation. Unlike the existing self-attention models [27], [30]–[37], we make use of the special structure of OM-Net, in order to provide cross-task guidance for the learning of category-specific channel attention.

### III. METHOD

In this section, we first show a strong segmentation baseline based on MC, and then introduce the model structure and training strategy for OM-Net. Next, we further explain the principle of OM-Net from the perspective of the attention mechanism, and propose the CGA module that promotes the performance of OM-Net via predicting robust channel attention. Finally, we propose a simple but effective post-processing method so as to refine the segmentation results of the attention network.

#### A. A Strong Baseline based on Model Cascade

According to [3], there are the following tumor classes: edema (ED), necrotic (NCR), non-enhancing tumor (NET), and enhancing tumor (ET). Following [38], we consistently merge NCR and NET into one class. Performance is evaluated on three re-defined tumor regions: complete tumor (including all tumor classes), tumor core (including all tumor classes except edema), and enhancing tumor (including the enhancing tumor class only). With such definition, three regions satisfy the hierarchical structure of tumor subregions, each of which completely covers its following one. Based on this observation, brain tumor segmentation can be decomposed into three individual yet relevant tasks. In the following, we design an MC model that includes three independent networks as a strong baseline for OM-Net. Each network is trained for a specific task. The three tasks are detailed in the following paragraph.

1) *Coarse segmentation of the complete tumor.* We utilize the first network to detect the complete tumor region as an ROI. We sample training patches randomly within the brain. To avoid overfitting, the network is trained as a more challenging *five-class segmentation task*: three tumor classes, normal tissue, and background. In the testing stage, it is still employed for binary segmentation by merging the predicted probabilities of all tumor classes. 2) *Refined segmentation for complete tumor and its intra-tumoral classes.* We dilate the above coarse

tumor mask by 5 voxels in order to reduce false negatives. Next, labels of all voxels in the dilated region are predicted again *as a five-class segmentation task* by the second network. Training data are sampled randomly within the dilated ground-truth complete tumor area. 3) *Precise segmentation for enhancing tumor.* Due to extreme class imbalance, precise segmentation of enhancing tumor is very difficult. To handle this problem, the third network is introduced specially for the segmentation of enhancing tumor. Similarly, training patches for this task are sampled randomly within the ground-truth tumor core area.

The network structure for the above three tasks is the same except for the final classification layer. The adopted structure is a 3D variant of the FusionNet [39], as shown in Fig. 1. We crop MRI images to patches of size  $32 \times 32 \times 16 \times 4$  voxels as input for the network, where the first three numbers correspond to the input volume and the last number 4 means the four MRI modalities. Due to the lack of contextual information, segmentation results of boundary voxels in the patch may be inaccurate. Therefore, we adopt the overlap-tile strategy proposed in [9] during inference. In brief, we only retain the predictions for voxels in the center region ( $20 \times 20 \times 5$ ) of the patch and abandon predictions for boundary voxels. This strategy is also utilized in the following models.

During the inference stage of MC, the three networks have to be run one-by-one since the ROI of one task is obtained by considering the results of all its preceding tasks. Specifically, we employ the first network to generate a coarse mask for the complete tumor. Then, all voxels within the dilated area of the mask are classified by the second network, from which the precise complete tumor and tumor core areas are obtained. Finally, the third network is utilized to scan all voxels in the tumor core region again to determine the precise enhancing tumor area. Thus, there are three alternate GPU-CPU computations carried out during the inference process of MC.

#### B. One-pass Multi-task Network

Despite its promising performance, MC not only has disadvantages in system complexity but also neglects the relevance among tasks. We observe that the essential difference among these tasks lies in training data rather than model architecture. Therefore, we propose a multi-task learning model that integrates the three tasks in MC into one network. Each task in this model has its own training data that is exactly the same as that in MC. Moreover, each task owns an independent convolutional layer, a classification layer, and a loss layer, respectively. The other parameters are shared to make use of the correlation among the tasks. Benefitting from the multi-task model, we can obtain the prediction results of the three classifiers simultaneously by one-pass computation. As a result, we name the proposed model as One-pass Multi-task Network (OM-Net).

As the three tasks are of increasing difficulty levels, we propose to train OM-Net more effectively based on curriculum learning [40], which is useful for improving the convergence quality of machine learning models. Specifically, instead of

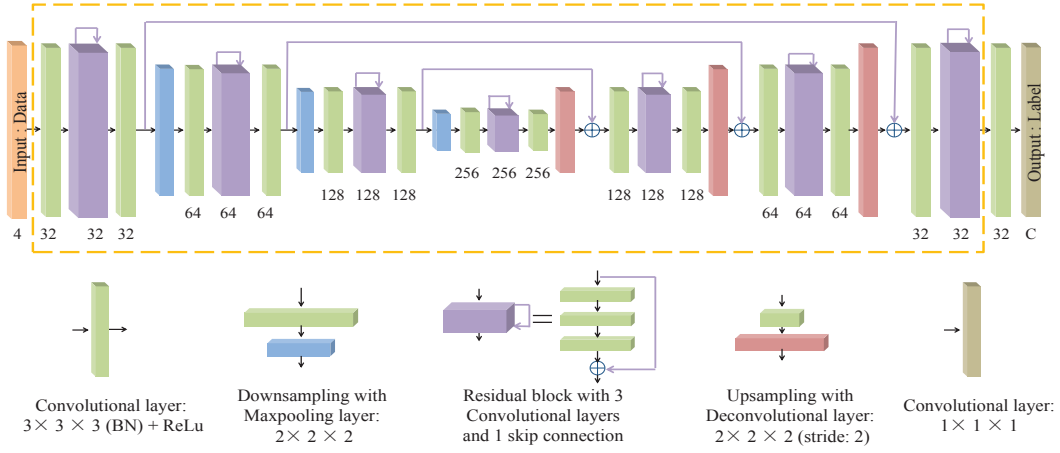


Fig. 1. Network structure for each task, which is composed of five basic building blocks. Each block is represented by one type of colored cube. The number below each cube refers to the number of feature maps.  $C$  equals to 5, 5, and 2 for the first, second, and third task, respectively. SoftmaxWithLoss is adopted as the loss function and applied to the output of each task. (Best viewed in color)

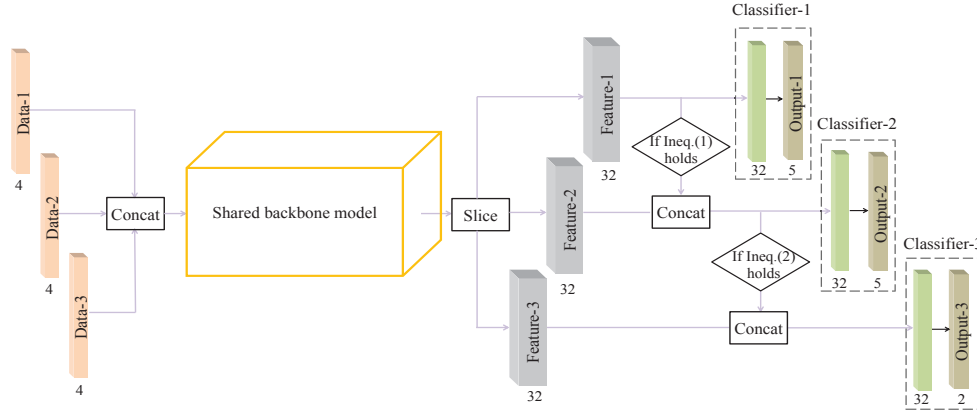


Fig. 2. Network structure of OM-Net in the training stage. For the  $i$ -th task, its training data, feature maps, and output of the classification layer are denoted as Data- $i$ , Feature- $i$ , and Output- $i$ , respectively. SoftmaxWithLoss is adopted as the loss function and applied to the output of each task. The shared backbone model refers to the network layers outlined by the yellow dashed line in Fig. 1.

training the three tasks together all the time, we gradually introduce the tasks to the model in an order of increasing difficulty level. Model structure and training strategy of OM-Net are illustrated in Fig. 2. First, OM-Net is trained with the first task only to learn the basic knowledge of differentiating tumor and normal tissues. This training process lasts until the loss curve tends to flatten.

The second task is then added to OM-Net. As illustrated in Fig. 2, we concatenate Data-1 and Data-2 along the batch dimension as the input for OM-Net. We slice features generated by the shared backbone model along the batch dimension where the slicing position is the same as the concatenation position. Then we obtain task-specific features and use the sliced features to optimize task-specific parameters. Moreover, we argue that not only knowledge (model parameters) but also learning material (training data), can be transferred from the easier course (task) to the more difficult course (task) in curriculum learning. Specifically, we propose the following online training data transfer strategy. Training patches in Data-1 that satisfy the following sampling condition can be

transferred to assist the training of the second task:

$$\frac{\sum_{i=1}^N \mathbf{1}\{l_i \in C_{complete}\}}{N} \geq 0.4, \quad (1)$$

where  $l_i$  is the label of the  $i$ -th voxel in the patch,  $C_{complete}$  denotes the set of all tumor classes,  $N$  is the number of voxels in the input patch, and 0.4 is set to meet the patch sampling condition of the second task. Thus, we concatenate the features of these patches in Data-1 with Feature-2 and then compute the loss for the second task. The training process in this step continues until the loss curve of the second task tends to flatten.

Finally, the third task and its training data are introduced to OM-Net. The concatenation and slicing operations are similar to those in the second step. Training patches from Data-1 and Data-2 that satisfy the following sampling condition can be transferred to the third task:

$$\frac{\sum_{i=1}^N \mathbf{1}\{l_i \in C_{core}\}}{N} \geq 0.5, \quad (2)$$

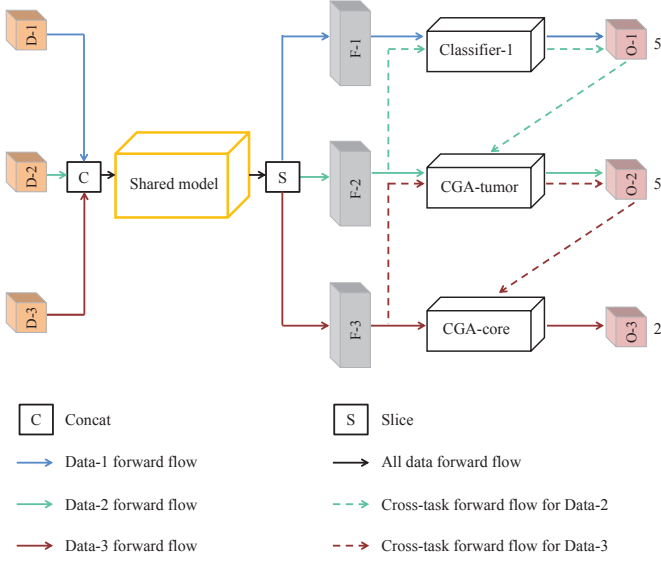


Fig. 3. The overall architecture of OM-Net equipped with CGA modules in the training stage.  $D-i$ ,  $F-i$ , and  $O-i$  are abbreviations of Data- $i$ , Feature- $i$ , and Output- $i$ , which denote training data, feature, and output for the  $i$ -th task, respectively. SoftmaxWithLoss is adopted as the loss function and applied to the output of each task. Feature-2 and Feature-3 pass through the first and second task respectively, to obtain their own coarse prediction results beforehand. We refer to the two operations as cross-task forward flow for Data-2 and Data-3, respectively. These coarse predictions are utilized as cross-task guidance to help generate category-specific channel attention. The training data transfer strategy described in Fig. 2 is omitted for clarity in this figure.

where  $C_{core}$  indicates the tumor classes that belong to tumor core. Similarly, 0.5 is chosen to meet the patch sampling condition of the third task. The three tasks are trained together until convergence. In conclusion, the OM-Net equipped with the curriculum learning-based training strategy has three main components: 1) a deep model based on multi-task learning that realizes coarse-to-fine segmentation by one-pass computation; 2) step-wise training scheme from easy to hard; 3) training data transfer from the easier task to the more difficult task.

In the inference stage, the data concatenation, feature slicing, and data transfer operations in Fig. 2 are removed. 3D patches of an MRI image are fed into the shared backbone model. Feature-1, Feature-2, and Feature-3 are now the same for each patch. Prediction results of the three tasks can be obtained simultaneously by OM-Net. The way to fuse these results is exactly the same as that in the MC baseline. Besides, OM-Net is different from the existing multi-task learning models for brain tumor segmentation [41], [42]. The principle of these models [41], [42] is to provide multiple supervisions for the same training data. In contrast, OM-Net aims to achieve coarse-to-fine segmentation by integrating tasks with their own training data into a single model.

### C. Cross-task Guided Attention

The coarse-to-fine segmentation strategy adopted by OM-Net can be regarded as a type of cascaded spatial attention, since segmentation results of one task determine the ROI for the following task. In the following, we further enhance the performance of OM-Net from the perspective of channel attention. Particularly, we propose a novel and

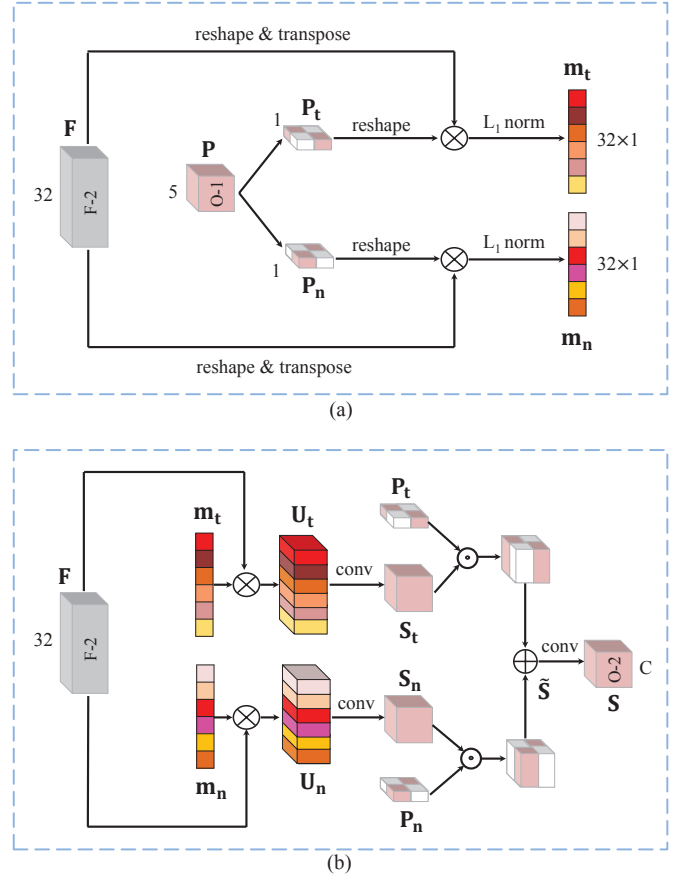


Fig. 4. Structure of the CGA-tumor module. (a) Category-specific channel importance (CSCI) block; (b) complementary segmentation (CompSeg) block. Elements in  $m_t$  and  $m_n$  describe the importance of each channel for one category of voxels within the patch, which are utilized to recalibrate channel-wise feature responses.

effective channel attention model, which makes use of cross-task guidance to solve the problems of the popular SE block for the segmentation task.

As explained in Section II, the global average pooling (GAP) operation in the SE block ignores the dramatic variation of each class in volume within the input patch. We solve this problem by computing statistics in category-specific regions, rather than in a whole patch. However, category-specific regions are unknown for common CNNs unless we reach the final classification layer. Therefore, it is a chicken-and-egg problem. Fortunately, OM-Net allows us to estimate category-specific regions beforehand by sharing prediction results between tasks. Specifically, in the training stage, we let Feature-2 and Feature-3 shown in Fig. 2 pass through the first and second task of OM-Net, respectively. In this way, we obtain the coarse segmentation results for the second and third tasks, respectively. It is worth noting that this strategy only introduces negligible additional computation in the training stage but no extra computation in the testing stage. This is because Feature-1, Feature-2, and Feature-3 are exactly the same in the testing stage as the concatenation and slicing operations in Fig. 2 are removed during testing. Since we introduce cross-task guidance for the proposed channel attention

block, we name it Cross-task Guided Attention (CGA). We also rename Classifier-2 and Classifier-3 in Fig. 2 equipped with CGA as CGA-tumor and CGA-core, respectively. The overall architecture of OM-Net equipped with CGA modules is illustrated in Fig. 3. Note that cross-task guidance takes place only in the forward pass, meaning that back-propagations of the three tasks are still independent.

As illustrated in Fig. 4, we take CGA-tumor as an example to illustrate the structure of the CGA module, which is composed of two blocks: (a) category-specific channel importance (CSCI) block, and (b) complementary segmentation (CompSeg) block. In Fig. 4, all 4D feature maps and probability maps are simplified to 3D cubes for better visualization. In particular, the height of one cube denotes the number of channels in feature maps.  $\mathbf{P} \in \mathbb{R}^{W \times H \times L \times 5}$  denotes a probability tensor predicted by the preceding task and is represented as a pink cube. The number 5 beside the cube for  $\mathbf{P}$  means the number of classes, which we have explained in the MC baseline. The grey cube  $\mathbf{F} \in \mathbb{R}^{W \times H \times L \times 32}$  denotes the input feature maps of the current task for the CGA module. The number 32 beside the cube for  $\mathbf{F}$  means its number of channels.

1) *CSCI Block*: As illustrated in Fig. 4 (a), the CSCI block utilizes both  $\mathbf{P}$  estimated by the preceding task and  $\mathbf{F}$  to estimate the importance of each channel for the segmentation of tumor and non-tumor categories, respectively. Specifically, we first compute  $\mathbf{P}_t$  and  $\mathbf{P}_n$ , whose each value refers to the probability of one voxel belonging to the tumor and non-tumor categories, respectively:

$$\mathbf{P}_t(i, j, k) = \sum_{c \in C_{tumor}} \mathbf{P}(i, j, k, c), \quad (3)$$

$$\mathbf{P}_n(i, j, k) = \sum_{c \in C_{non-tumor}} \mathbf{P}(i, j, k, c), \quad (4)$$

where  $\{\mathbf{P}_t, \mathbf{P}_n\} \in \mathbb{R}^{W \times H \times L \times 1}$ .  $C_{tumor}$  and  $C_{non-tumor}$  refer to the sets of classes that belong to tumor and non-tumor categories, respectively.  $C_{tumor}$  includes all tumor classes.  $C_{non-tumor}$  contains normal tissue and background. We then reshape  $\mathbf{P}_t$  and  $\mathbf{P}_n$  to  $\mathbb{R}^{N \times 1}$ , respectively, where  $N$  equals to  $W \times H \times L$  and denotes the number of voxels in a patch. Similarly,  $\mathbf{F}$  is reshaped to  $\mathbb{R}^{N \times 32}$ . Afterwards, we perform matrix multiplication between the reshaped  $\mathbf{F}$  and the reshaped  $\mathbf{P}_t$ , and apply  $L_1$  normalization for the obtained vector:

$$\mathbf{m}_t(i) = \frac{Re(\mathbf{F})^T_{i,:} \cdot Re(\mathbf{P}_t)}{\sum_{k=1}^{32} Re(\mathbf{F})^T_{k,:} \cdot Re(\mathbf{P}_t)}, \quad (5)$$

where  $\mathbf{m}_t \in \mathbb{R}^{32 \times 1}$ , and  $Re(\cdot)$  denotes the reshape operation. Similarly,

$$\mathbf{m}_n(i) = \frac{Re(\mathbf{F})^T_{i,:} \cdot Re(\mathbf{P}_n)}{\sum_{k=1}^{32} Re(\mathbf{F})^T_{k,:} \cdot Re(\mathbf{P}_n)}. \quad (6)$$

Elements in  $\mathbf{m}_t$  and  $\mathbf{m}_n$  describe the importance of each channel for the segmentation of tumor and non-tumor categories, respectively. Compared with the popular SE block that

squeezes global information of each channel into a single value to describe its importance, CGA makes use of finer category-specific statistics to evaluate the importance of each channel for one specific category.

2) *CompSeg Block*: Inspired by [43], we further propose a complementary segmentation (CompSeg) block that performs segmentation via two complementary pathways. As shown in Fig. 4 (b), the two pathways focus on the segmentation of the tumor and non-tumor voxels, respectively. Details of the CompSeg block are described as follows. First,  $\mathbf{m}_t$  and  $\mathbf{m}_n$  are used to recalibrate each channel in  $\mathbf{F}$ , respectively:

$$\mathbf{U}_t = \mathcal{F}_{scale}(\mathbf{m}_t, \mathbf{F}) = [m_t^1 \mathbf{f}_1, m_t^2 \mathbf{f}_2, \dots, m_t^{32} \mathbf{f}_{32}], \quad (7)$$

$$\mathbf{U}_n = \mathcal{F}_{scale}(\mathbf{m}_n, \mathbf{F}) = [m_n^1 \mathbf{f}_1, m_n^2 \mathbf{f}_2, \dots, m_n^{32} \mathbf{f}_{32}], \quad (8)$$

where  $\mathbf{f}_i \in \mathbb{R}^{W \times H \times L}$  is the  $i$ -th channel in  $\mathbf{F}$ .  $m_t^i$  and  $m_n^i$  are the  $i$ -th element in  $\mathbf{m}_t$  and  $\mathbf{m}_n$ , respectively. The recalibrated feature maps  $\mathbf{U}_t$  and  $\mathbf{U}_n$  highlight more important channels and suppress less important ones for tumor and non-tumor, respectively. They are then individually fed into a  $1 \times 1 \times 1$  convolutional classification layer to produce their own score maps  $\mathbf{S}_t$  and  $\mathbf{S}_n$ .  $\{\mathbf{S}_t, \mathbf{S}_n\} \in \mathbb{R}^{W \times H \times L \times C}$ , where  $C$  refers to the number of classes for the current task. The two score maps are more sensitive to tumor and non-tumor classes respectively with regard to all voxels. Therefore, we merge the two score maps by weighted averaging:

$$\tilde{\mathbf{S}}(i, j, k, c) = \mathbf{P}_t(i, j, k) \cdot \mathbf{S}_t(i, j, k, c) + \mathbf{P}_n(i, j, k) \cdot \mathbf{S}_n(i, j, k, c), \quad (9)$$

where  $\tilde{\mathbf{S}} \in \mathbb{R}^{W \times H \times L \times C}$ . Finally, we feed  $\tilde{\mathbf{S}}$  into another  $1 \times 1 \times 1$  convolutional layer to get the ultimate prediction results  $\mathbf{S}$  for the current task.

As illustrated in Fig. 4,  $\mathbf{P}_t$  and  $\mathbf{P}_n$  are used twice in CGA module. For the first time, we use  $\mathbf{P}_t$  and  $\mathbf{P}_n$  in the CSCI block to provide category-specific probabilities, by which we calculate  $\mathbf{m}_t$  and  $\mathbf{m}_n$  that embed the interdependencies between channels with regard to different categories, respectively. For the second time, we use them in the CompSeg block as soft spatial masks to merge two score maps by weighted averaging and produce the final segmentation results. Thanks to the integration of all tasks in OM-Net, we are able to obtain  $\mathbf{P}_t$  and  $\mathbf{P}_n$  as cross-task guidance to compute category-specific statistics for each channel and finally obtain better channel attentions. In comparison, the popular SE block ignores category-specific statistics and reweights each channel with a single weight. In the experimentation section, we justify effectiveness of the CSCI block and the CompSeg block, respectively.

Model structures of the CGA-tumor and CGA-core modules are exactly the same. There are only two trivial and intuitive differences. As illustrated in Fig. 3, the first difference lies in the position where we introduce the cross-task guidance. For the CGA-core module, it is introduced from the second task of OM-Net. Second, counterparts of  $\mathbf{P}_t$  and  $\mathbf{P}_n$  in CGA-core indicate the probability of each voxel belonging to the core and non-core tumor categories, respectively.

#### D. Post-processing

We observe from many studies [5]–[7], [11], [12], [51], [52] that post-processing is an efficient way to improve segmentation performance by refining the results of CNNs. For example, some small clusters of the predicted tumors are removed in [5], [12], [51], [52]. In addition, conditional random field (CRF) is commonly used as a post-processing step in [6], [7]. Particularly, Zhao *et al.* [11] proposed a post-processing method including six steps to boost the segmentation performance by a large margin.

In this paper, we introduce a simple and flexible post-processing method, in order to refine the predictions of the proposed networks. Our method is mainly inspired by [11], but it consists of fewer steps and adopts K-means clustering to achieve automatic classification instead of defining thresholds of voxel intensities in [11].

Step 1: We remove isolated small clusters whose volumes are smaller than a threshold  $\tau_{VOL}$ .  $\tau_{VOL} = \min(2000, 0.1 \times V_{max})$ , where  $V_{max}$  denotes the volume of the largest 3D connected tumor area predicted by the proposed model. This step can slightly improve the Dice score for complete tumor as false positives are removed.

Step 2: It is observed that non-enhancing voxels are likely to be misclassified as edema, if the predicted enhancing tumor area is small [11]. We propose a K-means-based method to handle this problem, as follows.

Let  $vol_e$  and  $vol_t$  denote the volumes of enhancing tumor and complete tumor in the predicted results, respectively.  $vol_e(n)$  and  $vol_t(n)$  refer to the volumes of enhancing tumor and complete tumor in the  $n$ -th 3D connected tumor area, respectively. If  $vol_e/vol_t < 0.1$ ,  $vol_e(n)/vol_t(n) < 0.05$ , and  $vol_e(n) < 1000$ , the K-means clustering algorithm is employed. Based on their intensity values in the MRI images, the segmented edema voxels in the  $n$ -th connected component are clustered into two groups. Finally, the average intensity of each group in the T1c channel is computed. We convert the labels of voxels in the group whose averaged intensity is lower to the non-enhancing class. Labels of voxels in the other group remain unchanged.

In the experiment section, we show that the second step significantly improves the Dice score of tumor core. As this step only changes the labels of the predicted edema voxels, it will not affect the segmentation results of complete tumor or enhancing tumor.

### IV. EXPERIMENTAL SETUP

We provide in this section the datasets we used to validate our approaches, the evaluation metrics, as well as implementation details.

#### A. Datasets

To show the effectiveness of the proposed methods, we conduct experiments on the BraTS 2018 [3], [44]–[47], BraTS 2017 [3], [44]–[46], and BraTS 2015 [3], [48] datasets. For each MRI image, there are four modalities: FLAIR, T1-weighted (T1), T1 with gadolinium enhancing contrast (T1c), and T2-weighted (T2). All images in the three datasets have

been co-registered, interpolated and skull-stripped. The dimensions of all images are  $240 \times 240 \times 155$  voxels.

The BraTS 2018 dataset contains three subsets: the training set, testing set, and validation set. The training set is composed of 210 cases of high-grade gliomas (HGG) and 75 cases of low-grade gliomas (LGG). The testing and validation sets contain 191 cases and 66 cases with hidden ground-truth, respectively. Evaluation metrics of the testing and validation sets are computed by an online evaluation platform [49].

The BraTS 2017 dataset shares the identical training set with BraTS 2018. Compared with BraTS 2018, it has a smaller validation set that comprises 46 cases. Evaluation of the validation set is conducted online [49].

The BraTS 2015 dataset consists of a training set including 274 MRI images and a testing set including 110 MRI images. Performance evaluation of the testing set is also conducted by an online evaluation platform [50].

#### B. Evaluation Metrics

We follow the official evaluation metrics for each dataset. Multiple metrics exist, i.e., Dice score, Positive Predictive Value (PPV), Sensitivity, and Hausdorff distance, defined respectively as below:

$$Dice = \frac{2TP}{FP + 2TP + FN}, \quad (10)$$

$$PPV = \frac{TP}{FP + TP}, \quad (11)$$

$$Sensitivity = \frac{TP}{TP + FN}, \quad (12)$$

$$Haus(T, P) = \max\{\sup_{t \in T} \inf_{p \in P} d(t, p), \sup_{p \in P} \inf_{t \in T} d(t, p)\}, \quad (13)$$

where the number of false negative, true negative, true positive, and false positive voxels are denoted as FN, TN, TP, and FP, respectively.  $\sup$  represents the supremum and  $\inf$  denotes the infimum.  $t$  and  $p$  denote the points on the surface  $T$  of the ground-truth regions and the surface  $P$  of the predicted regions, respectively.  $d(\cdot, \cdot)$  is the function that computes the distance between points  $t$  and  $p$ . Dice score, PPV, and Sensitivity measure voxel-wise overlap between the ground-truth and the predicted results [3]. Hausdorff distance evaluates the distance between the surface of the ground-truth regions and that of the predicted regions. Besides, Hausdorff95 is a metric of Hausdorff distance to measure the 95% quantile of the surface distance. As Dice score is the overall evaluation metric, adopted consistently across all the BraTS challenges, we adopt it as the main metric for evaluation following existing works [5]–[7], [11], [12], [15], [23], [35], [35], [41], [42], [47], [51], [52].

#### C. Implementation Details

For pre-processing, we normalize the voxel intensities within the brain area to have zero mean and unit variance for each MRI modality. The number of training patches is around 400,000, 400,000, and 200,000 for the first, second, and third task, respectively. SoftmaxWithLoss is adopted as

the loss function consistently. All implementations are based on the *C3D*<sup>1</sup> [53]–[55] package that is a modified 3D version of *Caffe* [55]. The models are trained using stochastic gradient descent with a momentum of 0.99, and a batchsize of 20 for each task. The initial learning rate of all networks is set as 0.001. Then it is divided by 2 after every 4 epochs. We train each network in MC for 20 epochs. Similarly, we train OM-Net for 1 epoch, 1 epoch, and 18 epochs for its three steps, respectively.

## V. EXPERIMENTAL RESULTS AND DISCUSSION

We first carry out ablation studies to show the validity of each contribution proposed in this paper. Then, we compare the performance of the proposed methods with state-of-the-art brain tumor segmentation approaches on the BraTS 2015, 2017, and 2018 datasets.

### A. Ablation Studies

The training set of BraTS 2018 is randomly divided into two subsets for convenient evaluation. The two subsets are a training subset and a local validation subset, which consist of 260 MRI images and 25 MRI images, respectively. Quantitative results of this local validation subset are presented in Table I. Here the one-model, two-model, and three-model cascades are denoted as MC1, MC2, and MC3, respectively. First, we can observe that with an increase of model number in MC, Dice scores improve steadily. These results prove the contribution of each deep network in MC. Unfortunately, the number of parameters increases with more models, which leads to more storage consumption and system complexity.

Second, we compare the performance of OM-Net with that of MC. With only one-third of the parameters of MC3, OM-Net obtains better segmentation performance consistently, especially for Dice scores on tumor core and enhancing tumor. Besides, we additionally train OM-Net<sup>0</sup> (a naive multi-task learning model without step-wise training or training data transfer) and OM-Net<sup>d</sup> (a multi-task learning model without step-wise training but with training data transfer). In Table I, OM-Net outperforms both OM-Net<sup>0</sup> and OM-Net<sup>d</sup>, which justifies the effectiveness of the data transfer strategy and the curriculum learning-based training strategy. In addition, we apply the proposed post-processing operation to refine the results of OM-Net, denoted as OM-Net<sup>p</sup>. Compared with OM-Net, it is shown that OM-Net<sup>p</sup> can slightly improve the Dice score for complete tumor due to false positives having been removed in the first post-processing step, and meanwhile, it significantly improves the Dice score of tumor core by 2.6%, because of the second post-processing step.

Third, to compare the performance of the CGA module with the SE block, we further test the OM-Net + SE model where an SE block is inserted before each Classifier- $i$  ( $1 \leq i \leq 3$ ) module of OM-Net in Fig. 2. Experimental results also show that OM-Net + CGA outperforms both OM-Net and OM-Net + SE consistently. Particularly, it outperforms OM-Net by as much as 2.28% on Dice score for the tumor core region.

TABLE I  
ABLATION STUDIES ON THE LOCAL VALIDATION SUBSET OF BRA TS  
2018 (%)

Method	Parameters	Dice		
		Complete	Core	Enhancing
MC1	13.813 M	90.41	78.48	72.91
MC2	27.626 M	91.08	79.11	75.14
MC3	41.439 M	91.08	79.11	79.53
OM-Net	13.869 M	91.10	79.87	<b>80.87</b>
OM-Net <sup>0</sup>	13.869 M	90.40	79.41	79.96
OM-Net <sup>d</sup>	13.869 M	91.11	79.93	80.26
OM-Net <sup>p</sup>	13.869 M	91.28	82.50	80.84
OM-Net + SE	13.870 M	91.03	80.20	80.72
OM-Net + CGA	13.814 M	91.34	82.15	80.73
OM-Net + CGA <sup>−</sup>	13.814 M	91.06	80.28	80.78
OM-Net + CGA <sup>p</sup>	13.814 M	<b>91.59</b>	<b>82.74</b>	80.73

In comparison, there is no clear difference in performance between OM-Net and OM-Net + SE. This can be explained from two perspectives. First, the GAP operation in the SE block ignores category-specific statistics. Second, recalibrating each channel with the same weight for all categories is suboptimal for segmentation. The proposed CGA module effectively handles the above two problems; therefore, it achieves better performance than the SE block. Besides, the model size of OM-Net + CGA is smaller than both OM-Net and OM-Net + SE. We can thus safely attribute the performance gains to the CGA module rather than to more parameters.

Fourth, we further make more experimental investigation into the CGA module, in order to prove the validity of the CSCI block and the CompSeg block respectively. As shown in Fig. 5, we visualize some feature maps produced by the shared backbone model. It should be noted that for intuitive and clear visualization, we choose to visualize the feature maps of a complete 2D slice rather than those of a 3D patch. To achieve this, we stitch F-2 and O-1 in Fig. 3 of all 3D patches in one MRI image. Then we select the feature maps  $\mathbf{F}$  and probability map  $\mathbf{P}$  of a certain slice, and calculate  $\mathbf{m}_t$  and  $\mathbf{m}_n$  corresponding to the slice according to Eq. 5 and Eq. 6, respectively. The channels corresponding to the largest 5 values and the smallest 5 values in  $\mathbf{m}_t$  are presented in Fig. 5 (c) and Fig. 5 (d), respectively. Similarly, the channels with the largest 5 values and the smallest 5 values in  $\mathbf{m}_n$  are presented in Fig. 5 (e) and Fig. 5 (f), respectively. Due to deconvolution layers used in the model, there are inevitable checkboard artifacts, but they do not affect observations.

It is clear that the feature maps shown in Fig. 5 (c) indeed have strong responses for the tumor region, which should be highlighted for the segmentation of the tumor. In contrast, the feature maps in Fig. 5 (d) have weak responses for the tumor region but strong responses for the non-tumor region; therefore, they will be suppressed in CGA for the segmentation of the tumor region. Similarly, consistent observations can be

<sup>1</sup><https://github.com/facebook/C3D>



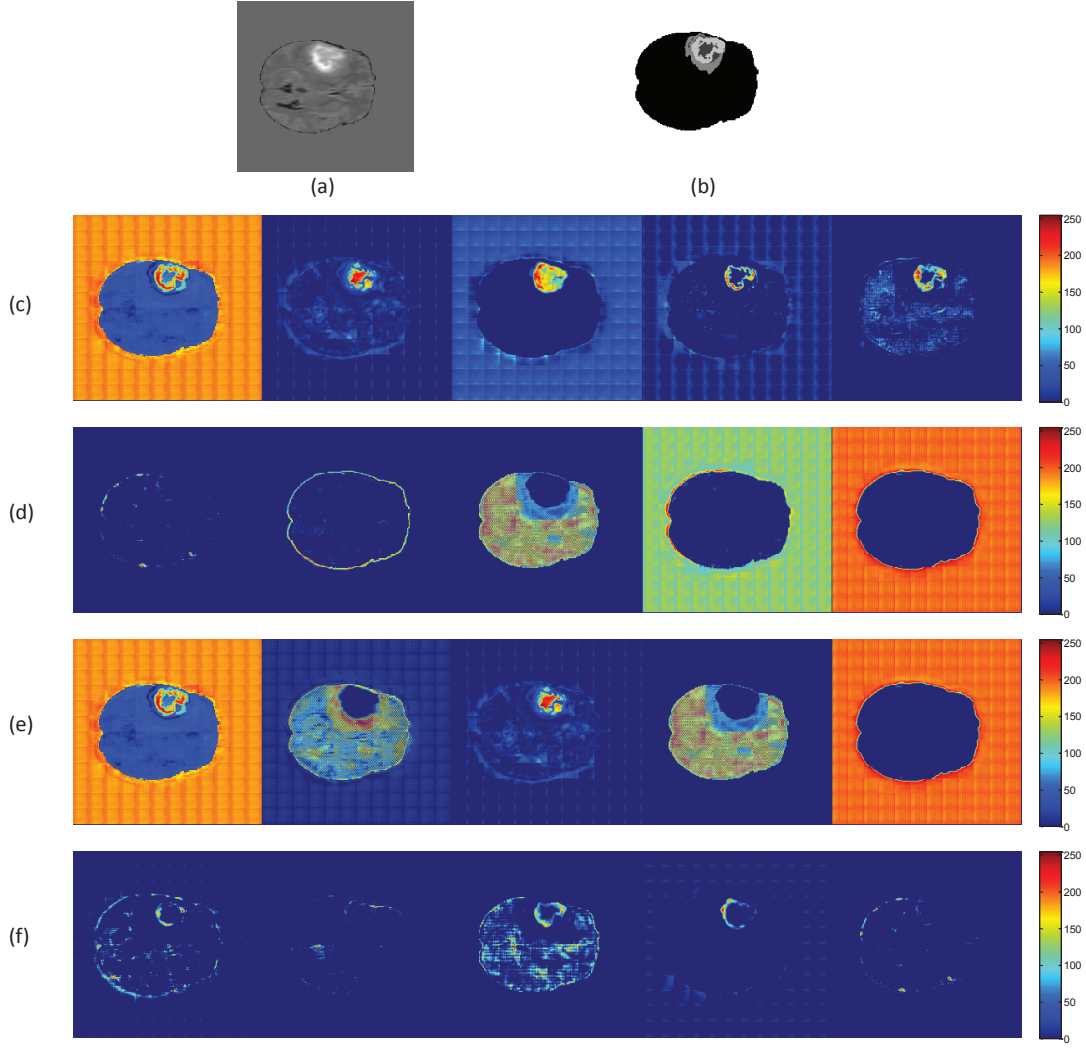


Fig. 5. Visualization of the output feature maps by the shared backbone model in OM-Net + CGA. We show the feature maps of a complete 2D slice for intuitive and clear visualization. (a) The Flair modality on the 75<sup>th</sup> slice of the sample *BraTS18\_2013\_21\_1* in the BraTS 2018 training set. (b) Its corresponding ground truth. (c) Heat maps corresponding to the channels with the largest 5 values in  $\mathbf{m}_t$ . (d) Heat maps corresponding to the channels with the smallest 5 values in  $\mathbf{m}_t$ . (e) Heat maps corresponding to the channels with the largest 5 values in  $\mathbf{m}_n$ . (f) Heat maps corresponding to the channels with the smallest 5 values in  $\mathbf{m}_n$ .

found in Fig. 5 (e) and Fig. 5 (f). The above analysis proves the validity of the CSCI block to generate the category-specific channel dependence.

Besides, we also justify the effectiveness of  $\mathbf{P}_t$  and  $\mathbf{P}_n$  as soft weights in the CompSeg block. We denote the model that simply performs an element-wise addition between  $\mathbf{S}_t$  and  $\mathbf{S}_n$  in Fig. 4 as OM-Net + CGA<sup>-</sup>. Experimental results in Table I show that OM-Net + CGA significantly outperforms OM-Net + CGA<sup>-</sup>. This is because OM-Net + CGA employs soft spatial masks ( $\mathbf{P}_t$  and  $\mathbf{P}_n$ ) to fuse two complementary prediction results. The above performance comparison proves the validity of the CompSeg block.

Finally, we utilize the proposed post-processing method to refine the segmentation results of both OM-Net and OM-Net + CGA, denoted as OM-Net<sup>p</sup> and OM-Net + CGA<sup>p</sup> in Table I, respectively. It is shown that post-processing brings in performance promotion for complete tumor and tumor core regions consistently. In conclusion, the above experimental

results justify the effectiveness of the proposed techniques. Qualitative comparisons between MC3, OM-Net, OM-Net + CGA, and OM-Net + CGA<sup>p</sup> are also provided in Fig. 6. It is clear that the proposed methods steadily improve the quality of brain tumor segmentation. This is consistent with the quantitative comparisons in Table I.

#### B. Performance Comparison on BraTS 2015 Testing Set

In this experiment, the performance of MC3, OM-Net, and OM-Net + CGA is evaluated on the testing set of the BraTS 2015 dataset. Each of them is trained using the entire training set of the dataset. Experimental results are tabulated in Table II. We have the following observations.

First, we compare the segmentation performance of MC3, OM-Net, OM-Net + CGA, and OM-Net + CGA<sup>p</sup>. It is shown that OM-Net has clear advantages over MC3, with 1% higher Dice scores on both tumor core and enhancing tumor. OM-Net + CGA further promotes the Dice score of OM-Net by 1% on

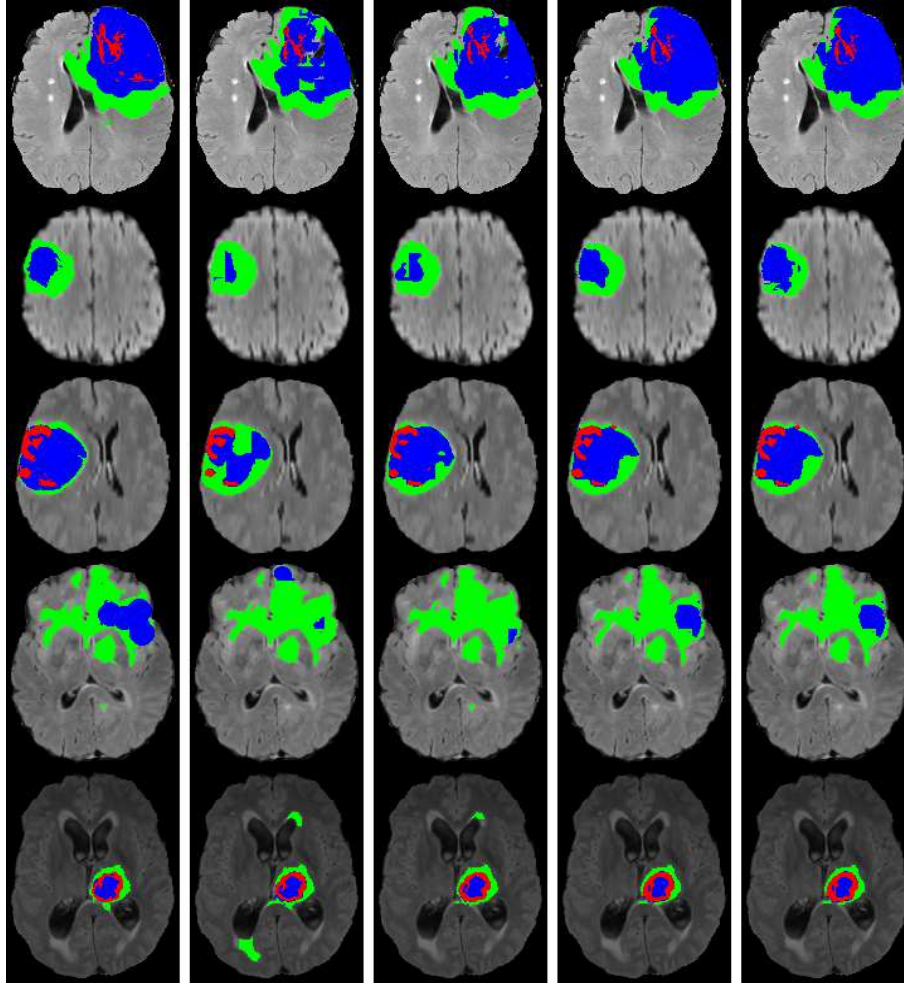


Fig. 6. Example segmentation results on the local validation subset of BraTS 2018. From left to right: Ground truth, MC3, OM-Net, OM-Net + CGA, and OM-Net + CGA<sup>p</sup> results overlaid on FLAIR image; edema (green), necrosis and non-enhancing (blue), and enhancing (red).

enhancing tumor. Moreover, after refinement by the proposed post-processing method, the Dice scores of OM-Net + CGA improve significantly by 1% and 4% on complete tumor and tumor core, respectively. These results are consistent with comparisons on the local validation subset of BraTS 2018.

Second, we compare the performance of OM-Net + CGA<sup>p</sup> with state-of-the-art methods. Our results have clear advantages over state-of-the-art methods [7], [11], [51], [56]. In particular, our results outperform the popular DeepMedic model [7] by 2%, 8%, and 2% in Dice scores on complete tumor, tumor core, and enhancing tumor, respectively. Besides, OM-Net + CGA<sup>p</sup> also outperforms the method proposed in [11] which adopts more pre-processing and post-processing operations. By the time of this submission, OM-Net + CGA<sup>p</sup> ranks first on the online leaderboard of BraTS 2015, showing the effectiveness of the proposed methods.

### C. Performance Comparison on BraTS 2017 Validation Set

Since access to the testing set of BraTS 2017 is closed after the challenge, we evaluate the proposed methods on the online validation set and compare them with other participants in Table III.

First, we train MC3, OM-Net, OM-Net + SE, and OM-Net + CGA models, using the training subset of 260 MRI images. We have the following observations. OM-Net outperforms MC3, especially for the Dice scores on enhancing tumor. The SE block cannot improve the performance of OM-Net in terms of Dice scores. In fact, it reduces the Dice score of OM-Net by 1.18% on enhancing tumor. In comparison, OM-Net + CGA outperforms both OM-Net and OM-Net + SE with a significant margin. Specifically, its Dice scores are 1.88% and 2.09% higher than those of OM-Net on tumor core and enhancing tumor respectively, which again proves the effectiveness of the CGA module. Besides, OM-Net + CGA<sup>p</sup> considerably improves the Dice score on tumor core, which justifies the effectiveness of the proposed post-processing method.

Second, to further boost the performance of OM-Net + CGA, 10-fold cross-validation is performed. A similar strategy has been widely adopted in recent studies [12], [15], [52]. The obtained 10 models are ensembled, denoted as OM-Net + CGA\*. Table III shows that OM-Net + CGA\* obtains higher Dice scores consistently than OM-Net + CGA. We also apply the proposed post-processing method to OM-Net + CGA\*, denoted as OM-Net + CGA<sup>\*p</sup>. It is shown that the proposed

TABLE II  
PERFORMANCE ON BRATS 2015 TESTING SET (%)

Method	Dice			Positive Predictive Value			Sensitivity		
	Complete	Core	Enhancing	Complete	Core	Enhancing	Complete	Core	Enhancing
MC3	86	70	63	86	82	60	88	67	72
OM-Net	86	71	64	86	83	61	88	68	72
OM-Net + CGA	86	71	65	87	84	63	88	67	70
OM-Net + CGA <sup>P</sup>	<b>87</b>	<b>75</b>	<b>65</b>	89	85	63	88	73	70
Isensee <i>et al.</i> [56]	85	74	64	83	80	63	91	73	72
Chen <i>et al.</i> [51]	85	72	61	86	83	66	86	68	63
Zhao <i>et al.</i> [11]	84	73	62	89	76	63	82	76	67
Kamnitsas <i>et al.</i> [7]	85	67	63	85	86	63	88	60	67

TABLE III  
MEAN VALUES OF DICE AND HAUSDORFF95 MEASUREMENTS ON BRATS 2017 VALIDATION SET

Method	Dice			Hausdorff95		
	Enh.	Whole	Core	Enh.	Whole	Core
MC3	0.7424	0.8991	0.7937	4.9901	4.6085	8.5537
OM-Net	0.7534	0.9007	0.7934	3.6547	7.2524	8.4676
OM-Net + SE	0.7416	0.8997	0.7938	3.5115	6.2859	7.0154
OM-Net + CGA	0.7743	0.8988	0.8122	3.8820	4.8380	6.7953
OM-Net + CGA <sup>P</sup>	0.7743	0.9016	0.8320	3.8820	4.6663	6.7312
OM-Net + CGA <sup>*</sup>	0.7852	0.9065	0.8274	3.2991	4.4886	6.9896
OM-Net + CGA <sup>*</sup> P	<b>0.7852</b>	<b>0.9071</b>	<b>0.8422</b>	3.2991	4.3815	7.5614
Wang <i>et al.</i> [23]	0.7859	0.9050	0.8378	3.2821	3.8901	6.4790
MIC_DKFZ	0.7756	0.9027	0.8194	3.1626	6.7673	8.6419
inpm	0.7723	0.8998	0.8085	4.7852	9.0029	7.2359
xfeng	0.7511	0.8922	0.7991	4.7547	16.3018	8.6847
Kamnitsas <i>et al.</i> [12]	0.738	0.901	0.797	4.50	4.23	6.56

post-processing method improves the Dice score of OM-Net + CGA<sup>\*</sup> by as much as 1.48% for tumor core.

Third, we show comparisons between OM-Net + CGA<sup>\*</sup>P and state-of-the-art methods on the online validation leaderboard, which attracts more than 60 entries. It is clear that OM-Net + CGA<sup>\*</sup>P outperforms all the other methods in terms of Dice scores. It is worth noting that other top entries, e.g., Kamnitsas *et al.* [12], also ensembled multiple models to boost performance. Besides, Wang *et al.* [23] integrated nine single-view models from three orthogonal views to achieve excellent performance. The above comparisons justify the superiority of our proposed methods.

#### D. Performance Comparison on BraTS 2018 Dataset

We further make more comparisons on the BraTS 2018 dataset. As BraTS 2018 and 2017 share the same training dataset, we directly evaluate the same models in the previous experiments on the validation set of BraTS 2018. The BraTS 2018 Challenge is intense and attracts more than 100 entries

on the online validation leaderboard. Therefore, we only show comparisons between our methods and the top entries in Table IV. We have the following observations.

First, comparison results between MC3, OM-Net, OM-Net + SE, and OM-Net + CGA are consistent with those in Table III. We can see that OM-Net achieves better performance than MC3 on enhancing tumor with a visible margin. Besides, with only a single model and without post-processing, OM-Net is able to outperform more than 70% entries on the leaderboard. In addition, OM-Net + CGA outperforms OM-Net by 1.26% and 1.45% in Dice scores on tumor core and enhancing tumor, respectively. In comparison, SE cannot improve the performance of OM-Net in terms of Dice scores.

Second, by model ensemble and the post-processing operation, OM-Net + CGA<sup>\*</sup>P obtains higher Dice scores as expected. It achieves very competitive performance on the leaderboard. It is worth noting that cross-validation and model ensemble have also been widely performed in [15], [52]. The approach described in [15] also decomposed the multi-class brain tumor segmentation into three tasks. It achieved top performance with large patches of size  $160 \times 192 \times 128$  voxels as inputs of the network. This leads to considerable memory consumption; therefore, GPUs of 32GB memory size were employed to train its model in [15]. In comparison, OM-Net utilizes small patches of size  $32 \times 32 \times 16$  voxels; therefore, it is memory efficient and can be trained or deployed on low-cost GPU devices. We can conclude that OM-Net is very competitive and has its own advantages.

More impressively, benefitting from the techniques proposed in this paper, we obtained the joint third position among 64 teams on the testing set of BraTS 2018 Challenge<sup>2</sup>. Detailed results of the challenge are introduced in [47]. In conclusion, the effectiveness of the proposed methods is justified by comparisons on the above three datasets.

## VI. CONCLUSION

In this paper, we propose a novel model, OM-Net, for brain tumor segmentation tailored for handling the class imbalance problem. Unlike the popular MC framework, OM-

<sup>2</sup><https://www.med.upenn.edu/sbia/brats2018/rankings.html>

TABLE IV  
MEAN VALUES OF DICE AND HAUSDORFF95 MEASUREMENTS ON BRATS  
2018 VALIDATION SET

Method	Dice			Hausdorff95		
	Enh.	Whole	Core	Enh.	Whole	Core
MC3	0.7732	0.9015	0.8233	4.1624	4.7198	7.6082
OM-Net	0.7882	0.9034	0.8273	3.1003	6.5218	7.1974
OM-Net + SE	0.7791	0.9034	0.8259	2.9950	5.7685	6.4289
OM-Net + CGA	0.8027	0.9033	0.8399	3.4437	4.7609	6.4339
OM-Net + CGA <sup>P</sup>	0.8027	0.9052	0.8536	3.4437	4.6236	6.3892
OM-Net + CGA*	0.8112	0.9074	0.8461	2.8697	4.9105	6.6243
OM-Net + CGA* <sup>P</sup>	0.8111	0.9078	0.8575	2.8810	4.8840	6.9322
Myronenko [15]	0.8233	0.9100	0.8668	3.9257	4.5160	6.8545
SHealth	0.8154	0.9120	0.8565	4.0461	4.2362	7.2181
Isensee <i>et al.</i> [52] <sup>†</sup>	0.8048	0.9072	0.8514	2.81	5.23	7.23
MedAI	0.8053	0.9104	0.8545	3.6695	4.1369	5.9821
BIGS2	0.8054	0.9104	0.8506	2.7543	4.8444	7.4548
SCAN	0.7925	0.9008	0.8474	3.6035	4.0626	4.9885

<sup>†</sup> For fair comparion, we report the performance of [52] without private training data.

Net requires only one-pass computation to perform coarse-to-fine segmentation. OM-Net is superior to MC because it not only significantly reduces the model size and system complexity, but also thoroughly exploits the correlation between the tasks by sharing parameters, training data, and even prediction results. In particular, we propose the CGA module that makes use of cross-task guidance information to learn category-specific channel attention, which outperforms the popular SE block significantly. In addition, we introduce a novel and effective post-processing method, with which the segmentation results can be refined to achieve better accuracy. Extensive experiments have been conducted on three popular datasets. Experimental results prove the effectiveness of the proposed OM-Net model and show that OM-Net has clear advantages over existing state-of-the-art methods for brain tumor segmentation.

## REFERENCES

- [1] A. Işın, C. Direkçioğlu, and M. Şah, "Review of MRI-based brain tumor image segmentation using deep learning methods," *Procedia Comput. Sci.*, vol. 102, pp. 317–324, 2016.
- [2] E. G. Van Meir, C. G. Hadjipanayis, A. D. Norden, H.-K. Shu, P. Y. Wen, and J. J. Olson, "Exciting new advances in neuro-oncology: the avenue to a cure for malignant glioma," *CA: a cancer journal for clinicians*, vol. 60, no. 3, pp. 166–193, 2010.
- [3] B. H. Menze, A. Jakab, S. Bauer, J. Kalpathy-Cramer, K. Farahani, J. Kirby, Y. Burren, N. Porz, J. Slotboom, R. Wiest *et al.*, "The multimodal brain tumor image segmentation benchmark (BRATS)," *IEEE Trans. Med. Imag.*, vol. 34, no. 10, pp. 1993–2024, 2015.
- [4] S. Bauer, R. Wiest, L.-P. Nolte, and M. Reyes, "A survey of MRI-based medical image analysis for brain tumor studies," *Phys. Med. Biol.*, vol. 58, no. 13, pp. R97–R129, 2013.
- [5] S. Pereira, A. Pinto, V. Alves, and C. A. Silva, "Brain tumor segmentation using convolutional neural networks in MRI images," *IEEE Trans. Med. Imag.*, vol. 35, no. 5, pp. 1240–1251, 2016.
- [6] M. Havaei, A. Davy, D. Warde-Farley, A. Biard, A. Courville, Y. Bengio, C. Pal, P.-M. Jodoin, and H. Larochelle, "Brain tumor segmentation with deep neural networks," *Med. Imag. Anal.*, vol. 35, pp. 18–31, 2017.

- [7] K. Kamnitsas, C. Ledig, V. F. Newcombe, J. P. Simpson, A. D. Kane, D. K. Menon, D. Rueckert, and B. Glocker, "Efficient multi-scale 3D CNN with fully connected CRF for accurate brain lesion segmentation," *Med. Imag. Anal.*, vol. 36, pp. 61–78, 2017.
- [8] J. Long, E. Shelhamer, and T. Darrell, "Fully convolutional networks for semantic segmentation," in *Proc. IEEE Conf. Comput. Vis. Pattern Recognit.*, 2015, pp. 3431–3440.
- [9] O. Ronneberger, P. Fischer, and T. Brox, "U-net: Convolutional networks for biomedical image segmentation," in *Proc. Int. Conf. Med. Image Comput. Comput.-Assist. Intervent*, 2015, pp. 234–241.
- [10] H. Chen, Q. Dou, L. Yu, J. Qin, and P.-A. Heng, "VoxResNet: Deep voxelwise residual networks for brain segmentation from 3D MR images," *NeuroImage*, vol. 170, pp. 446–455, 2018.
- [11] X. Zhao, Y. Wu, G. Song, Z. Li, Y. Zhang, and Y. Fan, "A deep learning model integrating FCNNs and CRFs for brain tumor segmentation," *Med. Imag. Anal.*, vol. 43, pp. 98–111, 2018.
- [12] K. Kamnitsas, W. Bai, E. Ferrante, S. McDonagh, M. Sinclair, N. Pawlowski, M. Rajchl, M. Lee, B. Kainz, D. Rueckert *et al.*, "Ensembles of multiple models and architectures for robust brain tumour segmentation," in *Proc. Int. Conf. Med. Image Comput. Comput.-Assist. Intervent Brainlesion Workshop*, 2017, pp. 450–462.
- [13] M. Saha and C. Chakraborty, "Her2Net: A deep framework for semantic segmentation and classification of cell membranes and nuclei in breast cancer evaluation," *IEEE Trans. Image Process.*, vol. 27, no. 5, pp. 2189–2200, 2018.
- [14] A. Farag, L. Lu, H. R. Roth, J. Liu, E. Turkbey, and R. M. Summers, "A bottom-up approach for pancreas segmentation using cascaded superpixels and (deep) image patch labeling," *IEEE Trans. Image Process.*, vol. 26, no. 1, pp. 386–399, 2017.
- [15] A. Myronenko, "3D MRI brain tumor segmentation using autoencoder regularization," *arXiv preprint arXiv: 1810.11654*, 2018.
- [16] H. Fehri, A. Gooya, Y. Lu, E. Meijering, S. A. Johnston, and A. F. Frangi, "Bayesian polytrees with learned deep features for multi-class cell segmentation," *IEEE Trans. Image Process.*, 2019.
- [17] D. Xiang, H. Tian, X. Yang, F. Shi, W. Zhu, H. Chen, and X. Chen, "Automatic segmentation of retinal layer in OCT images with choroidal neovascularization," *IEEE Trans. Image Process.*, vol. 27, no. 12, pp. 5880–5891, 2018.
- [18] M. Haghighi, S. K. Warfield, and S. Kurugol, "Automatic renal segmentation in DCE-MRI using convolutional neural networks," in *Proc. IEEE Int. Symposium on Biomed. Imag. (ISBI)*, 2018, pp. 1534–1537.
- [19] H. Hu, Q. Guan, S. Chen, Z. Ji, and L. Yao, "Detection and recognition for life state of cell cancer using two-stage cascade CNNs," *IEEE/ACM Trans. Comput. Biol. Bioinf.*, 2017.
- [20] P. F. Christ, M. E. A. Elshaer, F. Ettlinger, S. Tatavarty, M. Bickel, P. Bilic, M. Rempfler, M. Armbruster, F. Hofmann, M. DAnastasi *et al.*, "Automatic liver and lesion segmentation in CT using cascaded fully convolutional neural networks and 3D conditional random fields," in *Proc. Int. Conf. Med. Image Comput. Comput.-Assist. Intervent*, 2016, pp. 415–423.
- [21] Z. Zhu, Y. Xia, W. Shen, E. K. Fishman, and A. L. Yuille, "A 3D coarse-to-fine framework for automatic pancreas segmentation," *arXiv preprint arXiv:1712.00201*, 2017.
- [22] N. Lessmann, B. van Ginneken, M. Zreik, P. A. de Jong, B. D. de Vos, M. A. Viergever, and I. Išgum, "Automatic calcium scoring in low-dose chest CT using deep neural networks with dilated convolutions," *IEEE Trans. Med. Imag.*, vol. 37, no. 2, pp. 615–625, 2018.
- [23] G. Wang, W. Li, S. Ourselin, and T. Vercauteren, "Automatic brain tumor segmentation using cascaded anisotropic convolutional neural networks," in *Proc. Int. Conf. Med. Image Comput. Comput.-Assist. Intervent Brainlesion Workshop*, 2017, pp. 178–190.
- [24] J. Zhang, M. Liu, and D. Shen, "Detecting anatomical landmarks from limited medical imaging data using two-stage task-oriented deep neural networks," *IEEE Trans. Image Process.*, vol. 26, no. 10, pp. 4753–4764, 2017.
- [25] Y. Tang and X. Wu, "Scene text detection and segmentation based on cascaded convolution neural networks," *IEEE Trans. Image Process.*, vol. 26, no. 3, pp. 1509–1520, 2017.
- [26] J. Guo, W. Zhu, F. Shi, D. Xiang, H. Chen, and X. Chen, "A framework for classification and segmentation of branch retinal artery occlusion in SD-OCT," *IEEE Trans. Image Process.*, vol. 26, no. 7, pp. 3518–3527, 2017.
- [27] J. Hu, L. Shen, and G. Sun, "Squeeze-and-excitation networks," in *Proc. IEEE Conf. Comput. Vis. Pattern Recognit.*, 2018.
- [28] C. Zhou, C. Ding, Z. Lu, X. Wang, and D. Tao, "One-pass multi-task convolutional neural networks for efficient brain tumor segmentation," in *Proc. Int. Conf. Med. Image Comput. Comput.-Assist. Intervent*, 2018, pp. 637–645.

- [29] P. Krähenbühl and V. Koltun, “Efficient inference in fully connected crfs with gaussian edge potentials,” in *Proc. Adv. Neural Inf. Process. Syst.*, 2011, pp. 109–117.
- [30] M. Jaderberg, K. Simonyan, A. Zisserman *et al.*, “Spatial transformer networks,” in *Proc. Adv. Neural Inf. Process. Syst.*, 2015, pp. 2017–2025.
- [31] W. Li, X. Zhu, and S. Gong, “Harmonious attention network for person re-identification,” in *Proc. IEEE Conf. Comput. Vis. Pattern Recognit.*, vol. 1, 2018, p. 2.
- [32] F. Wang, M. Jiang, C. Qian, S. Yang, C. Li, H. Zhang, X. Wang, and X. Tang, “Residual attention network for image classification,” in *Proc. IEEE Conf. Comput. Vis. Pattern Recognit.*, 2017, pp. 6450–6458.
- [33] A. G. Roy, N. Navab, and C. Wachinger, “Concurrent spatial and channel squeeze & excitation in fully convolutional networks,” in *Proc. Int. Conf. Med. Image Comput. Comput.-Assist. Intervent*, 2018, pp. 421–429.
- [34] S. Woo, J. Park, J.-Y. Lee, and I. S. Kweon, “CBAM: Convolutional block attention module,” in *Proc. Eur. Conf. Comput. Vis.*, 2018.
- [35] S. Pereira, V. Alves, and C. A. Silva, “Adaptive feature recombination and recalibration for semantic segmentation: application to brain tumor segmentation in MRI,” in *Proc. Int. Conf. Med. Image Comput. Comput.-Assist. Intervent*, 2018, pp. 706–714.
- [36] Y. Zhu, C. Zhao, H. Guo, J. Wang, X. Zhao, and H. Lu, “Attention couplenet: Fully convolutional attention coupling network for object detection,” *IEEE Trans. Image Process.*, vol. 28, no. 1, pp. 113–126, 2019.
- [37] A. BenTaieb and G. Hamarneh, “Predicting cancer with a recurrent visual attention model for histopathology images,” in *Proc. Int. Conf. Med. Image Comput. Comput.-Assist. Intervent*. Springer, 2018, pp. 129–137.
- [38] Section for Biomedical Image Analysis, MICCAI BraTS 2018. [Online]. Available: <https://www.med.upenn.edu/sbia/brats2018/data.html>
- [39] T. M. Quan, D. G. Hilderbrand, and W.-K. Jeong, “Fusionnet: A deep fully residual convolutional neural network for image segmentation in connectomics,” *arXiv preprint arXiv:1612.05360*, 2016.
- [40] Y. Bengio, J. Louradour, R. Collobert, and J. Weston, “Curriculum learning,” in *Proc. Int. Conf. Mach. Learn. (ICML)*, 2009, pp. 41–48.
- [41] H. Shen, R. Wang, J. Zhang, and S. McKenna, “Multi-task fully convolutional network for brain tumour segmentation,” in *Annu. Conf. Med. Imag. Understand. Anal. (MIUA)*, 2017, pp. 239–248.
- [42] H. Shen, R. Wang, J. Zhang, and S. J. McKenna, “Boundary-aware fully convolutional network for brain tumor segmentation,” in *Proc. Int. Conf. Med. Image Comput. Comput.-Assist. Intervent*, 2017, pp. 433–441.
- [43] R. Dey and Y. Hong, “CompNet: Complementary segmentation network for brain MRI extraction,” in *Proc. Int. Conf. Med. Image Comput. Comput.-Assist. Intervent*, 2018, pp. 628–636.
- [44] S. Bakas, H. Akbari, A. Sotiras, M. Bilello, M. Rozycki, J. S. Kirby, J. B. Freymann, K. Farahani, and C. Davatzikos, “Advancing the cancer genome atlas glioma MRI collections with expert segmentation labels and radiomic features,” *Nat. Sci. Data*, vol. 4, p. 170117, 2017.
- [45] S. Bakas, H. Akbari, A. Sotiras, M. Bilello, M. Rozycki, J. Kirby, J. Freymann, K. Farahani, and C. Davatzikos, “Segmentation labels and radiomic features for the pre-operative scans of the TCGA-LGG collection,” *Cancer Imaging Arch.*, 2017.
- [46] S. Bakas, H. Akbari, A. Sotiras, M. Bilello, M. Rozycki, J. Kirby, J. Freymann, K. Farahani, and C. Davatzikos, “Segmentation labels and radiomic features for the pre-operative scans of the TCGA-GBM collection,” *Cancer Imaging Arch.*, 2017.
- [47] S. Bakas, M. Reyes, A. Jakab, S. Bauer, M. Rempfler, A. Crimi, R. T. Shinohara, C. Berger, S. M. Ha, M. Rozycki *et al.*, “Identifying the best machine learning algorithms for brain tumor segmentation, progression assessment, and overall survival prediction in the BRATS challenge,” *arXiv preprint arXiv:1811.02629*, 2018.
- [48] M. Kistler, S. Bonaretti, M. Pfahrer, R. Niklaus, and P. Büchler, “The virtual skeleton database: an open access repository for biomedical research and collaboration,” *J. Med. Internet Res.*, vol. 15, no. 11, 2013.
- [49] Center for Biomedical Image Computing and Analytics, University of Pennsylvania, “Image processing portal - <https://ipp.cbica.upenn.edu/>,” *A web accessible platform for imaging analytics*, 2015.
- [50] VirtualSkeleton, BRATS 2013 Sep. 30, 2015 [Online]. Available: <https://www.virtualskeleton.ch/BRATS/Start2015>
- [51] X. Chen, J. H. Liew, W. Xiong, C.-K. Chui, and S.-H. Ong, “Focus, segment and erase: An efficient network for multi-label brain tumor segmentation,” in *Proc. Eur. Conf. Comput. Vis.*, 2018, pp. 674–689.
- [52] F. Isensee, P. Kickingereder, W. Wick, M. Bendszus, and K. H. Maier-Hein, “No new-net,” in *Proc. Int. Conf. Med. Image Comput. Comput.-Assist. Intervent Brainlesion Workshop*, 2018, pp. 234–244.
- [53] D. Tran, L. Bourdev, R. Fergus, L. Torresani, and M. Paluri, “Learning spatiotemporal features with 3D convolutional networks,” in *Proc. IEEE Int. Conf. Comput. Vis.*, 2015, pp. 4489–4497.
- [54] A. Karpathy, G. Toderici, S. Shetty, T. Leung, R. Sukthankar, and L. Fei-Fei, “Large-scale video classification with convolutional neural networks,” in *Proc. IEEE Conf. Comput. Vis. Pattern Recognit.*, 2014, pp. 1725–1732.
- [55] Y. Jia, E. Shelhamer, J. Donahue, S. Karayev, J. Long, R. Girshick, S. Guadarrama, and T. Darrell, “Caffe: Convolutional architecture for fast feature embedding,” in *Proc. 22nd ACM Int. Conf. Multimedia*, 2014, pp. 675–678.
- [56] F. Isensee, P. Kickingereder, W. Wick, M. Bendszus, and K. H. Maier-Hein, “Brain tumor segmentation and radiomics survival prediction: Contribution to the BRATS 2017 challenge,” in *Proc. Int. Conf. Med. Image Comput. Comput.-Assist. Intervent Brainlesion Workshop*, 2017, pp. 287–297.